Picozzi, M., Bindi, D., Festa, G., Cotton, F., Scala, A., D'Agostino, N. (2022): Spatiotemporal Evolution of Microseismicity Seismic Source Properties at the Irpinia Near-Fault Observatory, Southern Italy. - Bulletin of the Seismological Society of America, 112, 1, 226-242.

https://doi.org/10.1785/0120210064

Spatiotemporal Evolution of Microseismicity Seismic Source Properties at the Irpinia Near-Fault Observatory, Southern Italy

Matteo Picozzi*[1], Dino Bindi[2], Gaetano Festa[1], Fabrice Cotton[2,3], Antonio Scala[1], and Nicola D'Agostino[4]

ABSTRACT

We estimate the source parameters of small-magnitude earthquakes that occurred during 2008–2020 in the Irpinia faults area (southern Italy). We apply a spectral decomposition approach to isolate the source contribution from propagation and site effects for ~3000 earthquakes in the local magnitude range between M_L 0 and 4.2. We develop our analyses in three steps. First, we fit the Brune (1970) model to the nonparametric source spectra to estimate corner frequency and seismic moment, and we map the spatial distribution of stress drop across the Irpinia area. We found stress drops in the range 0.4–8.1 MPa, with earthquakes deeper than 7 km characterized by higher average stress drop (i.e., 3.2 MPa). Second, assuming a simple stress-release model (Kanamori and Heaton, 2000), we derive fracture energy and critical slip-weakening distance. The spatial variability of stress drop and fracture energy allows us to image the present stress conditions of fault segments activated during the 23 November 1980 M_S 6.9 earthquake. The variability of the source parameters shows clear patterns of the fault mechanical properties, suggesting that the Irpinia fault system can be divided into three main sectors, with the northern and southern ones showing different properties from the central one. Our results agree with previous studies indicating the presence of fluids with different composition in the different sectors of the Irpinia fault system. In the third step, we compare the time evolution of source parameters with a time series of geodetic displacement recorded near the fault system. Temporal trends in the correlation between geodetic displacement and different source parameters indicate that the poroelastic deformation perturbation generated by the karst aquifer recharge is modulating not only the occurrence rate of microseismicity (D'Agostino et al., 2018) but may lead to rupture asperities with different sizes and characteristics.

Key points:

- We estimate seismic moment and corner frequency from microseismicity and study stress-drop variability.
- The studied fault system in southern Italy shows segmentation and characteristics varying with time.
- Seismic source parameters show high temporal correlation with geodetic displacement.

Supplemental Material

INTRODUCTION

The Campania–Lucania Apennine in southern Italy is a region characterized by frequent kilometric-scale ruptures capable of generating earthquakes up to magnitude 7 (Chiarabba et al., 2005; Improta et al., 2014), resulting in one of the highest seismic hazard areas of the Mediterranean region. The last large earthquake in this area is traced back to 23 November 1980, when the M_S 6.9 Irpinia earthquake took place along northwest–southeast-striking faults. Like other large earthquakes in Italy, the M_S 6.9 Irpinia earthquake was characterized by a complex rupture, consisting of three main rupture episodes occurring within a few seconds, which caused about 3000 fatalities and severe damage (Bernard and Zollo, 1989).

With the aim of mitigating the seismic risk in the Irpinia area, for the past 10 yr, the Irpinia Near-Fault Observatory (see Data and Resources) has been continuously monitoring in real time the region through the Irpinia Seismic Network (ISNet, see Data and Resources) (Fig. 1), composed of 31 seismic stations covering an area of 120 × 80 km^2 (Fig. 1a) including the epicenter of the 1980 Irpinia earthquake (Iannaccone et al., 2010; Vassallo et al., 2012).

One of the main goals of near-fault observatories is to improve our understanding of physical processes occurring within seismogenic volumes and their temporal and spatial evolution, to capture any preparatory process that anticipates large earthquakes. One means to achieve this goal is to monitor either changes in the mechanical properties of rocks hosting the faults, such as seismic velocity, or to retrieve seismic source parameters through the inversion of seismic data (e.g., Wang et al., 2019; Chiarabba et al., 2020).

Characterization of moderate to microearthquakes (i.e., events with magnitude <4) is therefore central for many reasons: to understand how faults slip, to infer the mechanical state of faults, and to constrain the physical and chemical processes that occur on them until the nucleation of a large event (e.g., Bentz et al., 2020; Durand et al., 2020).

Previous works have investigated the microseismicity characteristics in the Irpinia region (Cantore et al., 2011; Stabile et al., 2012; Zollo et al., 2014; Picozzi et al., 2019; Festa et al., 2021), showing that ISNet provides good-quality microearthquake recordings and fulfills the requirements provided by Kwiatek and Ben-Zion (2016) for unbiased estimates of source parameters (i.e., seismic moment, M_0, corner frequency, f_c, which combined lead to stress drop, $\Delta\sigma_S$). For example, Zollo et al. (2014) applied a parametric approach (e.g., Kawase, 2006; Shearer et al., 2006;

[1] Department of Physics, University of Naples Federico II, Naples, Italy, https://orcid.org/0000-0001-8078-9416 (MP); https://orcid.org/0000-0002-2588-8160 (GF); https://orcid.org/0000-0003-4584-463X (AS); [2] GFZ German Research Centre for Geosciences, Helmholtz Centre Potsdam, Telegrafenberg, Germany, https://orcid.org/0000-0002-8619-2220 (DB); https://orcid.org/0000-0002-9242-3996 (FC); [3] Institute for Earth and Environmental Sciences, University of Potsdam, Potsdam, Germany; [4] Istituto Nazionale Geofisica e Vulcanologia, Rome, Italy, https://orcid.org/0000-0002-0444-6240 (ND)

*Corresponding author: matteo.picozzi@unina.it

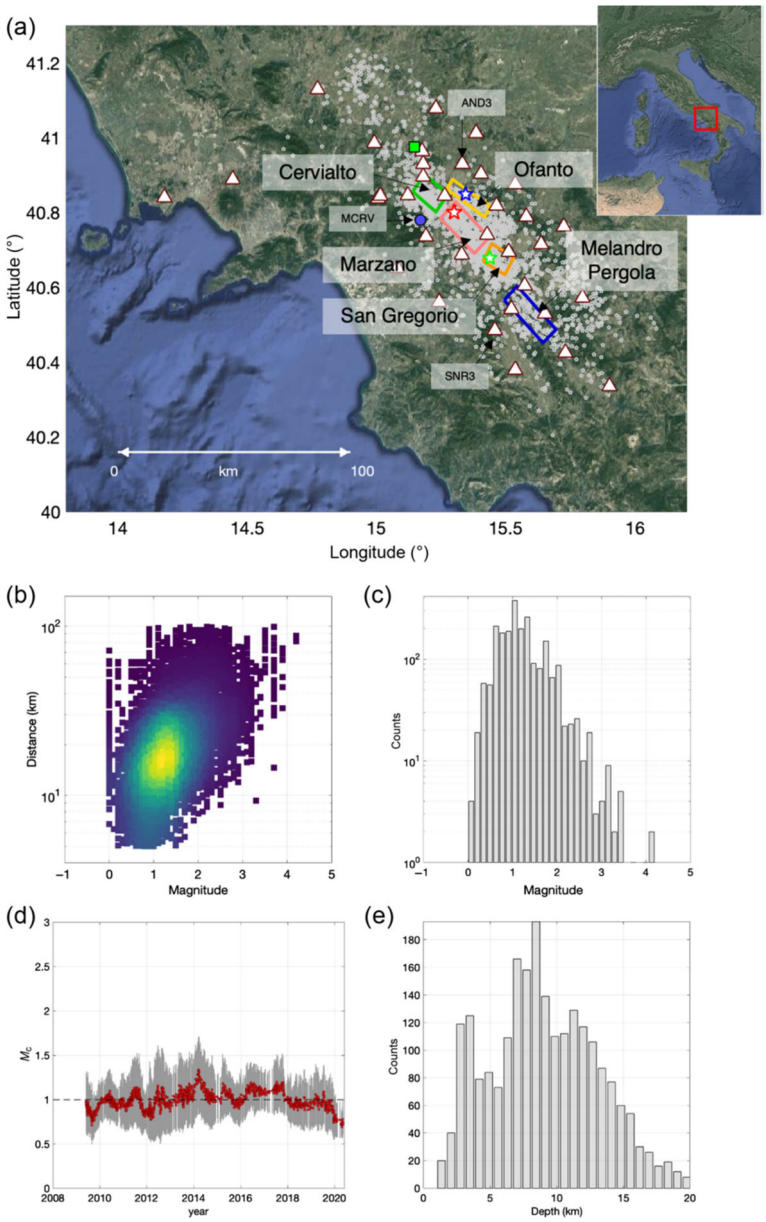

Figure 1. *(a) Locations of the earthquakes considered in this study (gray stars), Irpinia Seismic Network (ISNet) seismic stations (white triangles) and Global Navigation Satellite Systems (GNSS) station MRCV (blue circle). CO_2 degassing site Mefite d'Ansanto (green square). Projection of seismogenic sources: Cervialto fault (green line), Marzano fault (red line), S. Gregorio fault (orange line), Ofanto fault (yellow line), and Melandro–Pergola fault (cyan line). The 1980, M_w 6.9 Irpinia earthquake was characterized by three main rupture segments, nucleating at 0 s (red star), 20 s (green star) and 40 s (blue star). The inset shows the location of the study area within Italy. (b) Magnitude versus hypocentral distance scatter plot for the recordings analyzed in this study. (c) Histogram showing the distribution of magnitude for the considered events. (d) Temporal distribution of completeness magnitude ±1 standard deviation. (e) Histogram showing the distribution of hypocentral depths. The color version of this figure is available only in the electronic edition.*

Tsuda et al., 2010; Goertz-Allmann et al., 2011; Kwiatek et al., 2011, 2014; Ross and Ben-Zion, 2016) to study the source characteristics of about 700 microearthquakes in the seismic moment range $4 \times 10^9 - 2 \times 10^{14}$ N · m (i.e., magnitude between M_w 0.3 and 3.5). They found $\Delta\sigma_S$ varying between 0.1 and 10 MPa, with a median value of 1.4 MPa; they also found low Savage-Wood seismic efficiency and a relatively high ratio of S-wave to P-wave attenuation quality factor (i.e., Q_S/Q_P between 0.8 and 2.1). Similar results regarding $\Delta\sigma_S$ have been found by Festa et al. (2021) by analyzing the source properties of a seismic sequence that occurred in July 2020 at the northern tip of the main segment ruptured during the 1980 Irpinia earthquake (M_L ranging between M_w – 0.5 and 3.0).

Recently, Picozzi et al. (2019) estimated the radiated seismic energy (E_S) and seismic moment (M_0) of about 2300 earthquakes with magnitude M_w between 0.3 and 3.8 that occurred within a buffer of _30 km along the Irpinia fault system during the period 2008–2018. The authors investigated the temporal and spatial distribution of apparent stress (i.e., $\tau_a = \mu \cdot E_S/M_0$, in which μ is the rigidity of the source medium; Wyss and Brune, 1968). The spatial distribution of τ_a was found to well complement the velocity and attenuation images from Amoroso et al. (2014) and Improta et al. (2014), showing low values in the shallowest portion (i.e., within ~15 km) of the central sector in the Irpinia fault system that corresponds to highly fractured, fluid-filled carbonate rocks.

Upscaling analyses exploiting velocity and attenuation estimates led Amoroso et al. (2017) to estimate for the central sector of the Irpinia fault system a range of porosity in limestones between 4% and 5%, and a fluid composition consisting of brine–CO_2 and/or CH_4–CO_2. Picozzi et al. (2019) suggested that these crustal fluids may have influenced the observed long-term temporal variation for τ_a. On the other hand, D'Agostino et al. (2018) showed that microseismicity in the Irpinia area is also modulated by the crustal deformation of karst aquifers in limestones due to groundwater recharge.

The relevance of pore-pressure variations within fluid-filled cracks in driving background seismicity and promoting the nucleation of large earthquakes is well documented for the Apennine chain (e.g., Lucente et al., 2010; Improta et al., 2014; Sugan et al., 2014; Chiarabba et al., 2020). For example, the contribution of overpressured CO_2-rich fluids in the generation of the 2009 M_w 6.3 L'Aquila (central Apennines, Italy) earthquake has been suggested by Lucente et al. (2010) and Terakawa et al. (2010), among others.

Here, we consider events that occurred during the period from 26 February 2008 to 17 May 2020, for a total of 3016 earthquakes in the magnitude range M_L 0 and M_L 4.2.

This work is structured in different levels of detail regarding data analysis and the use of seismological models. First, we focus on the spatial distribution of source parameters (i.e., seismic moment M_0 and the corner frequency f_c) extracted from the nonparametric source spectra as provided by the spectral decomposition analysis. M_0 and f_c are used to estimate the source radius, the stress drop ($\Delta\sigma_S$), and the average slip per event, assuming a circular rupture model (Brune, 1970). The spatial distribution of these source parameters is also analyzed. Then, the rupture process is modeled as a frictional process through a simple stress-release model (Kanamori and Heaton, 2000), with which estimates of the fracture energy, EG, and critical slip-weakening distance, D_c, are obtained.

Finally, the temporal evolution of source parameters is studied with respect to geodetic displacement (following D'Agostino et al., 2018), paying attention to possible changes in the trend of these independent geophysical data, which could suggest changes in the behavior of the Irpinia fault system.

DATA SET

We analyze about 36,200 acceleration and velocity waveforms from 3016 earthquakes with magnitudes between M_L 0 and M_L 4.2 and recorded by at least three stations in the range of 2–100 km. Uncertainties in event locations (De Landro et al., 2015) are mostly within 1 km both horizontally and vertically (i.e., the median error in location is ~0:5 km). The magnitude versus hypocentral distance scatter plot of the data set analyzed in this study (Fig. 1b) and the distribution of magnitudes (Fig. 1c) show that the data set is dominated by microearthquakes with M_L between 0.5 and 2. The completeness magnitude M_c over the years is fairly stable around ML 1 (Fig. 1d; defined by the software package ZMAP, Wiemer, 2001), in agreement with the estimate of M_L 1.1 proposed by Vassallo et al. (2012). Figure 1d shows that the distribution of events with depth is rather broad, covering an interval between about 2 km and more than 20 km, with a higher density of events around 3 and 8 km. This distribution of hypocentral depths is linked to the rather complex geological structure of the Irpinia area (Matrullo et al., 2013; Bello et al., 2021), which is characterized by the presence of Apenninic carbonate platform and Lagonegro basin units overlying the Apulian carbonate units.

Data processing is performed following Picozzi et al. (2019) using velocimetric records sampled at 125 Hz. After deconvolution for the instrumental response, Fourier amplitude spectra (FAS) are computed considering 81 frequencies equally spaced in the logarithmic scale, in the range 0.1–50 Hz. Similar to Pacor et al. (2016), we consider time windows starting 0.1 s before the S-wave onset and ending at different percentages of the total energy depending on the source to site distance R: (1) 90% when $R < 25$ km, (2) 80% when 25 km $< R <$ 50 km, and (3) 70% when $R >$ 50 km. For FAS calculation, we impose a minimum time-window length of 5 s and a maximum length of 20 s. For each recording, the signal-to-noise ratio (SNR) is evaluated considering a pre-event noise window of the same length as the signal window. We consider FAS for the horizontal components, which are smoothed by a filter with variable frequency band equal to 25% of the central frequency and combined into their root mean square average. Data are extracted with the following criteria: hypocentral distance less than 100 km; events recorded by a minimum of three stations. A frequency-dependent SNR threshold is applied to select the Fourier amplitudes: SNR = 10 at low frequencies (0.2–0.4 Hz), SNR = 5 in the frequency range 0.4–15 Hz, and SNR = 10 at frequencies larger than 15 Hz. Thus, the actual number of frequencies used for source inversion varies between 24 and 35.

METHODS

Generalized inversion technique (GIT)

The first level of our analysis aims at isolating in the recorded signals the contribution of the source spectra in the recorded signals from path and site effects. For this purpose, we follow the strategy proposed by Picozzi et al. (2017) in which the GIT (Castro et al., 1990) is coupled with a genetic algorithm (GA) optimization approach (Yamanaka and Ishida, 1996). First, GIT is used to decompose recorded FAS in terms of source, propagation, and site contributions; then, the GA is applied to invert the obtained empirical source spectra and to explore the parameter space locally and globally for optimal solutions in terms of corner frequency (f_c) and seismic moment (M_0) source parameters.

The spectral decomposition is based on the assumption that the logarithm of the S-wave FAS can be modeled as a linear combination of the source spectra, S, the attenuation, A, and site response Z, that is

$$\log_{10} U_{ij}(f, r_{ij}) = \log_{10} S_i(f) + \log_{10} A(f, r_{ij}) + \log_{10} Z_j(f), \quad (1)$$

in which the symbols i and j indicate the ith earthquake and the jth station, respectively; f is the frequency, and r_{ij} is a measure of the hypocentral distance.

In this work, we used the processing procedure proposed by Oth et al. (2011), which consists of one-step GIT. For each frequency, the inversion is performed in a least-square sense (Paige and Saunders, 1982) and 200 bootstrap replications are considered to evaluate uncertainties (Efron, 1979). After some adjustments, the hypocentral distance interval from 2 to 52 km is discretized into 20 bins, each 2.5 km wide.

The nonparametric GIT does not require any a priori assumption about the functional form of the attenuation operator, which avoids assumptions about anelastic attenuation or geometrical spreading. On the other hand, two unresolved degrees of freedom concerning equation (1) must be removed by adding some constraints. The constraints adopted in this work are as follows: (1) for all frequencies, the attenuation operator is set to 1 at the reference hypocentral distance, $r_0 = 2$ km; (2) to eliminate the linear dependence between source and site, the average site amplification of a set of selected reference stations is set to one for all frequencies. In addition, we require the attenuation to vary smoothly with distance.

Following Cantore et al. (2011), we selected AND3 as a reference station. Because AND3 is located in the northeastern sector of ISNet, we added SRN3 as an additional reference station to cover the southwestern sector of the network. We refer to Castro et al. (1990), for details on the implementation of these constraints.

Source spectra inversion

Once the empirical source spectra $S(f)$ are obtained, we assume a model to describe the source rupture process in terms of seismic moment and corner frequency. Of course, considering one source model instead of another one makes the results study dependent, with possible effects both on the scaling with earthquake size between model's parameter (e.g., Oth et al., 2017; Trugman, 2020), and on ground-motion variability due to simplifications adopted to describe the effects of style of faulting, radiation pattern, and rupture velocity variability (Baltay et al., 2013; Causse and Song, 2015; Denolle and Shearer, 2016). In this work, we assume an ω^2 source model (Brune, 1970), in which the displacement source spectrum has the form:

$$S(f) = \frac{R^{\theta\varphi} V F}{4\pi\rho V_S^3 R_0} M(f) \tag{2}$$

$$M(f) = \frac{M_0}{1 + \left(\frac{f}{f_c}\right)^2}, \tag{3}$$

in which the term $R^{\theta\varphi}$ represents the S-wave average radiation pattern, set to 0.55 (Boore and Boatwright, 1984); the reference distance R_0 according to the GIT analysis is set to 2 km; the free-surface factor F is 2; V_S and ρ are the S-wave velocity and density in the source region, respectively. Regarding the latter parameters, we use for each event the values of V_S and density values at the hypocenter location extracted from the crustal model proposed by Matrullo et al. (2013).

In addition, similar to Oth et al. (2011), we correct the empirical source spectra for the high-frequency decay, which is not considered by the constraints adopted in the GIT inversion. To this end, we estimate for the reference station AND3 the κ_0 decay in the source spectra for events with magnitude $M_L \leq 2.5$ and for frequencies ≥10 Hz by fitting an exponential model as $S(f) = S_0 \exp(-\pi\kappa_0 f)$ (Anderson and Hough, 1984). The κ_0 estimates define a normal distribution with a mean value of 0.016 ± 0.012 s (Fig. S1a, available in the supplemental material to this article). This value of κ_0 is consistent with those expected for hard-rock sites at the Earth's surface (e.g., Hartzell et al., 1996; Boore, 2003). The κ_0 for the second reference station (SRN3) used in the GIT inversion is $0{:}043 \pm 0{:}016$ s.

Following Picozzi et al. (2017), a GA optimization approach is used to estimate M_0 and f_c from equation (3). For each empirical source inversion, we define a search domain in the parameter space related to M_0 and f_c depending on the event magnitude from the bulletin. We start with an initial population of 200 randomly generated individuals. Then, genetic operations (i.e., crossover, mutation, dynamic mutation, and elite selection) are used to obtain new populations of the same size, in which new individuals (models) reproduce based on the misfit of the previous generation. The crossover probability is set to 0.9, whereas the mutation probability is set to 0.05 at the beginning of the inversion, but this value changes dynamically during the iterations. The iterations are terminated at the 151th generation because it (1) corresponds to no further significant misfit reduction and (2) allows the GA to sample the parameter space around the global minimum at the price of a computational time of about 15 s per inversion.

A comprehensive description of the method and examples of its application can be found in Yamanaka and Ishida (1996) and Picozzi et al. (2017).

Although exploitative algorithms such as GAs remain less easily trapped in local minima than linearized approaches, they are less efficient in converging to the global minimum. To improve this aspect, Picozzi et al. (2017) proposed a new type of objective function that includes the partial derivatives of the source spectra with respect to source parameters, which allows the inversion to converge to the optimal solution. The inversion of each source spectrum is performed for 200 bootstrap replications associated with each inversion (Efron, 1979), and the parameter uncertainty is evaluated on the distribution of models with the best fit extracted at each replication.

Simple stress-release model and source parameters

In addition to the typical source information derived from M_0 and f_c (i.e., dimension of the sources, stress drop, and average slip), we exploit here M_0 and f_c in a simple stress-release model (Kanamori and Heaton, 2000) to derive source information describing the energy budget of the rupture processes. Starting with the estimates of M_0 and f_c, we compute the stress drop ($\Delta\sigma_S$) following Hanks and Thatcher (1972):

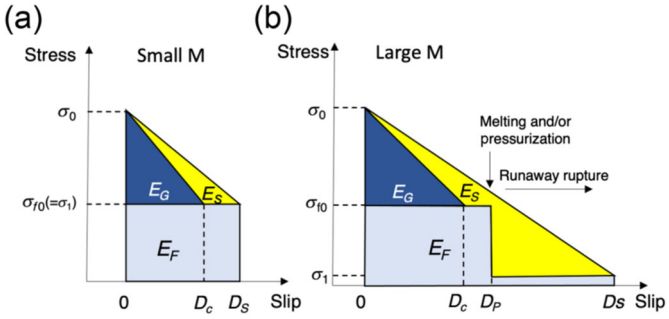

Figure 2. *Schematic stress release pattern for (a) small and (b) large earthquakes. Redrawn from Kanamori and Heaton (2000). The color version of this figure is available only in the electronic edition.*

$$\Delta\sigma_S = \frac{7M_0}{16R^3}, \tag{4}$$

in which R is the source radius. The seismic moment is defined as $M_0 = \mu D_S S$, with μ being the crustal shear modulus, D_S the average seismic slip, and S the fault surface. In this study, the crustal shear modulus μ varies with depth considering the velocity model proposed by Matrullo et al. (2013).

The source radius is computed using the Brune's model as a function of the corner frequency and the shear-wave velocity:

$$R = \frac{2.34V_S}{2\pi f_c}, \tag{5}$$

Following Eshelby (1957), the average seismic slip is

$$D_S = \left(\frac{16}{7}\right)^{\frac{2}{3}} \left(\frac{1}{\pi}\right) M_0^{\frac{1}{3}} \Delta\sigma_s^{\frac{2}{3}}/\mu, \tag{6}$$

and the radiated energy E_S using the theoretical S-wave source spectrum as proposed by Izutani and Kanamori (2001):

$$E_S = \frac{4\pi}{5\rho V_S^5} \int_0^\infty |CfS(f)|^2 df \text{ , with } C = \frac{\rho V_S^3 R_0}{\pi R^{\theta\varphi} VF}. \tag{7}$$

Furthermore, we consider a simple stress-release model (Fig. 2a) to derive and study the spatiotemporal evolution of other source parameters (Orowan, 1960; Savage and Wood, 1971; Kanamori and Heaton, 2000). In particular, starting from the energy budget

$$\Delta W = E_R + E_F + E_G, \tag{8}$$

in which ΔW is the strain energy drop, E_S the seismic radiated energy, E_F the frictional energy loss, and E_G the fracture energy. An estimate of E_G for the simple stress-release model considered can be obtained as (Kanamori and Heaton, 2000)

$$E_G = \frac{\Delta\sigma_S}{2}\frac{M_0}{\mu} - E_R. \tag{9}$$

Once the fracture energy is estimated, we can derive the critical slip-weakening distance

$$D_c = \frac{2E_G}{\Delta\sigma_S S}. \tag{10}$$

The schematic linear slip-weakening stress-release model shown in Figure 2a can change significantly in case of melting or pressurization (Fig. 2b). Indeed, if slip exceeds a given threshold D_p, melting and pressurization can contribute to a further reduction of the friction level and lead to runaway rupture (i.e., a large increase of the slip until barriers or other tectonic or geometric limits are found; Kanamori and Heaton, 2000). Considering the small magnitudes analyzed in this study, we limit our attention to the model in Figure 2a.

RESULTS

Level I. Seismic moment, corner frequency, and stress drop

The results of the inversion scheme given by the GIT and the GA on the data set of 3016 events are shown in Figure 3. The nonparametric spectral attenuation curves (Fig. 3a) show a clear frequency dependence, the attenuation being stronger for high frequencies, and decrease monotonically with hypocentral distance. The trends of the attenuation functions are bounded by the decays $1/r$ and $1/r^2$. Following Pacor et al. (2016), we fit the nonparametric attenuation function to obtain estimates of geometrical spreading and frequency-dependent quality factor, which are input parameters for ground-motion prediction and simulation (Boore, 1983). Because a detailed discussion of the attenuation parameters is not the primary objective of this work, the results of the nonparametric attenuation functions inversion are presented and discussed in the supplemental material (Fig. S2 and Text S1).

Figure 3b shows the empirical site functions from GIT. The site responses of ISNet stations show moderate to more prominent amplifications above ~3 Hz. According to Cantore et al. (2011), stations placed on soft soil show larger amplification (e.g., PGN3, CLT3, and CMP3). We consider site response an important but not a priority outcome of our study. Therefore, we provide the site response functions of all the stations in the supplemental material (Figs. S6–S35).

The empirical source spectra are shown in Figure 3c, used as input for the GA optimization. Chen and Abercrombie (2020) suggested the use of stacking approaches, such as the GIT applied in this work, to estimate source parameters. Indeed, with these approaches, reliable source parameter estimates can be obtained up to 80% of the maximum available frequency (i.e., having used 50 Hz as maximum frequency, the limit for considering estimates reliable would be 40 Hz). In this work, we discarded all solutions with misfit larger than 0.1 and, in agreement with Zollo et al. (2014), those with corner frequency higher than 45 Hz. This selection led us to reduce the interpretable source spectra to 2155, with only 67 exceeding the threshold suggested by Chen and Abercrombie (2020).

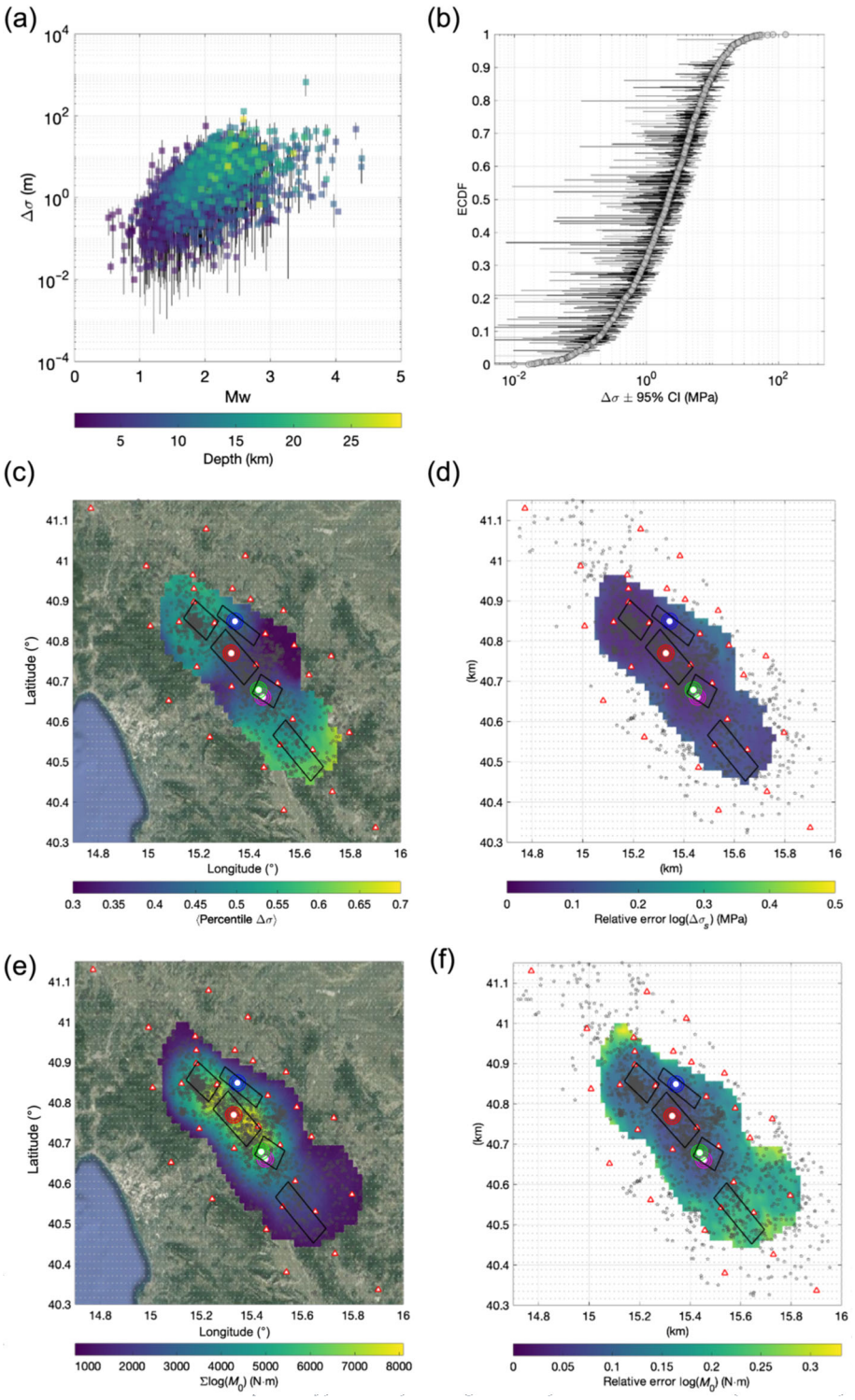

Figure 4. *a) $\Delta\sigma_S$ versus M_w with 95% CI (vertical black lines). Data are colored per hypocentral depth. (b) ECDF for $\Delta\sigma_S$ with the 95% probability CI. (c) Map showing the spatial distribution for the percentiles of $\Delta\sigma_S$. Panel (d) is same as panel (a), but for the relative error of Δσ. Panel (e) is same as panel (a), but for the cumulative of M_0. Panel (f) is same as panel (a), but for the relative error of M_0. The color version of this figure is available only in the electronic edition.*

Figure 3d shows the scaling relationship of source parameters f_c and M_0, with associated uncertainties. For completeness, we report in Figure 3e,f the empirical cumulative probability distribution (ECDF) of M_0 and f_c, respectively, along with their uncertainties. The relative error for f_c and M_0 is also shown in Figure S4, in which we can see that the two relative errors appear to be weakly correlated.

The variability of the source characteristics in terms of $\Delta\sigma_S$ (Fig. 3d) is quite large, with a mean value of 2.2 MPa and 16th and 84th percentiles of 0.4 and 8.1 MPa, respectively. A striking feature is the variability of $\Delta\sigma_S$ with the hypocentral depth, leading events to have higher $\Delta\sigma_S$ at larger depth, regardless of their seismic moment. Specifically, events with hypocentral depths shallower than 7 km and between 7 and 15 km have average $\Delta\sigma_S$ equal to 0.5 and 3.2 MPa, respectively (Fig. S4a,b). Although the variability of these two subsets is quite large (i.e., 16th and 84th percentiles equal to 0.1 and 2.3 and 1.0 and 9.3 MPa, respectively), we observe that the mean $\Delta\sigma_S$ 3.2 MPa for the 7–15 km depth interval is consistent with that estimated by Bernard and Zollo (1989) for the 1980 M_S 6.9 Irpinia earthquake, which enucleated at about 10 km of depth. A further striking evidence is that shallow earthquakes have a magnitude range between M_w 0.5 and M_w 3, whereas deeper sources correspond to magnitudes between M_w 1.2 and M_w 4.2 (Fig. S4). The variability of source characteristics in terms of $\Delta\sigma_S$ is also evident when looking at the different amplitudes of source spectra above 10 Hz for events with M_w equal to 2.5 ± 0.1 (Fig. 3c).

Following Oth (2013), we investigate the parameter ε which, as suggested by Kanamori and Rivera (2004), may allow us to quantify how strongly $\Delta\sigma$ varies with M_0 through the relation $M_0 \propto f_c^{-(3+\varepsilon)}$. We estimate ε for the entire data set, as well as for events with hypocentral depths smaller than 7 km, between 7 and 15 km, and for events with depths between 10 and 15 km and f_c > 20 Hz (the latter data set allows us to consider only events occurring at depth comparable to the 1980 Irpinia earthquake and with M_w > 1.5). The obtained values are: $\varepsilon = -0.75 \pm 0.29$ for the whole data set; $\varepsilon = -1.05 \pm 0.25$ for depths smaller than 7 km; $\varepsilon = -0.39 \pm 0.18$ for depths between 7 and 15 km; and $\varepsilon = -0.09 \pm 0.18$ for depths between 10 and 15 km (Fig. 3c). Considering the errors associated with the parameters ε, the null hypothesis of self-similar scaling cannot be rejected at 95% confidence level only for the last data set (i.e., depth between 10 and 15 km and f_c > 20 Hz). In other

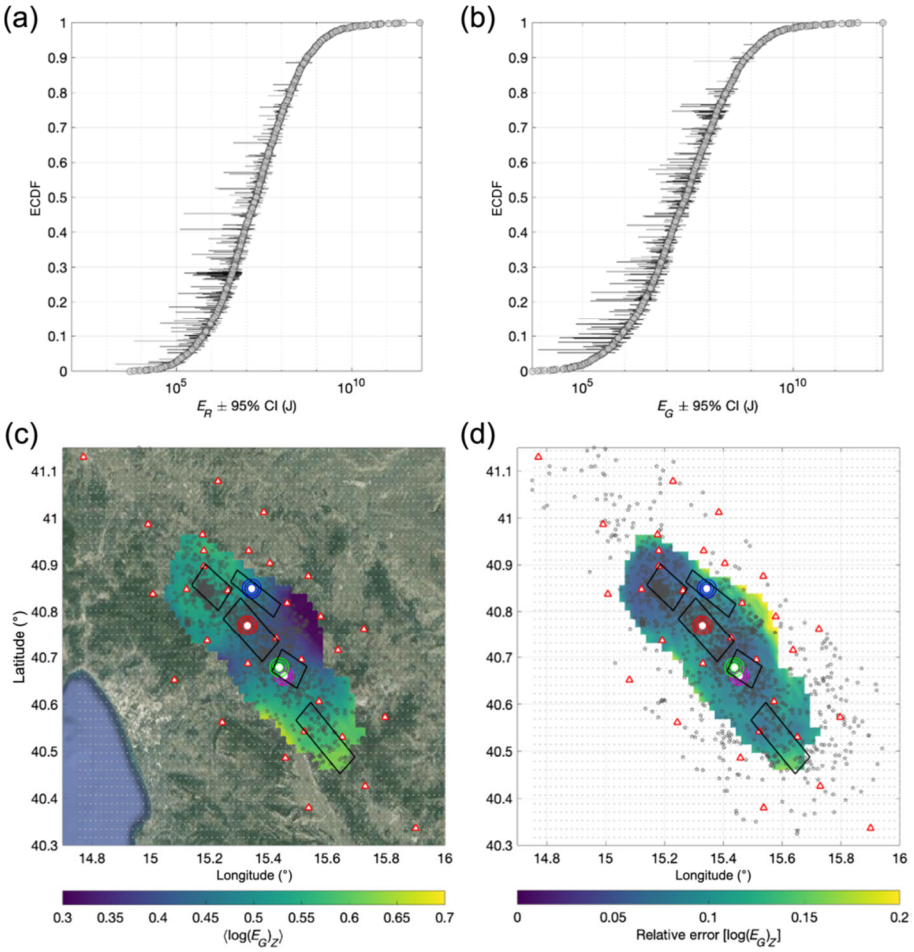

Figure 5. *(a) ECDF for E_R with the 95% probability CI. Panel (b) is same as panel (a), but for E_G. (c) Map showing the spatial distribution for the percentiles of $\log(E_G)Z$. Panel (d) is same as panel (a), but for the relative error of $\log(E_G)_Z$. The color version of this figure is available only in the electronic edition.*

words, only for the deepest and largest microseismicity, we can consider that the self-similarity holds and $\Delta\sigma_S$ is on average constant with M_0. Values of ε statistically different from zero have been found, for example, by Oth (2013) in Japan in response to different tectonic, faulting, and thermal crustal conditions. We will investigate this issue further in a dedicated study.

In Figure 4a, we show the distribution of $\Delta\sigma_S$ with respect to moment magnitude. The uncertainty on $\Delta\sigma_S$ is computed by propagating the errors affecting M_0 and f_c (Cotton et al., 2013; Bindi et al., 2018) as described in the Appendix. Figure 4b shows that the uncertainty on $\Delta\sigma_S$ does not limit our ability to observe the different properties of shallow events compared to those in the depth range compatible with the nucleation of the 1980 Irpinia earthquake.

Similarly to Picozzi et al. (2019), whose work explored for the Irpinia area the spatial variability of τ_a, we investigate whether the variability of $\Delta\sigma_S$ seen in Figures 3c and 4a corresponds to a specific spatial pattern of source rupture characteristics. A similar approach was used by Oth (2013) to study, at the scale of Japan as a whole, the relationship between variations in the earthquake stress release and variations in heat flux. Here, we focus on a much smaller area with the goal of assessing whether variations in stress release exist between fault segments of the same system. For this purpose, we follow an approach similar to Wiemer and Wyss (2002) and we map $\Delta\sigma_S$ in space by considering a regular 3D grid with size of 2 km. For each grid node, we compute the average ECDF values for $\Delta\sigma_S$ occurring within a maximum distance of 10 km. The results for nodes having less than 50 earthquakes within 10 km are not shown. Hence, our images provide insight into the spatial distribution of $\Delta\sigma_S$ anomalies with respect to the average value for the Irpinia area. Compared to tomographic images of velocity or anelastic parameters, our images are fully data driven and depend only on the data distribution and selected smoothing level. Furthermore, to assess the robustness of imaged values, we evaluate the uncertainties following a bootstrap approach (Efron, 1979).

Figure 4c,d) shows the mean percentile of $\Delta\sigma_S$ for 20 bootstrap iterations and the standard error associated with the estimates (similar maps for hypocentral depth in the range 0–7 and 7–15 km are shown in Fig. S5a,b, respectively). We observe clear spatial patterns in $\Delta\sigma_S$ (Fig 4c), with a large area of low values in the central sector of the Irpinia area (i.e., roughly corresponding to the Monte Marzano segment, in which the 1980 Irpinia earthquake nucleated, and to the Ofanto fault). We observe intermediate stress-drop values in the northern sector (i.e., along the Cervialto segment), which ruptured during the first episode of the 1980 Irpinia earthquake, and the largest ones in the southern sector (i.e., along the Melandro–Pergola segment), which is hypothesized to be the fault that hosted the 1857 M_w 7.0 Val D'Agri earthquake (Burrato and Valensise, 2008). The main fault segments in the Irpinia area are shown in Figure 1a. Figure 4d shows that the relative error associated with $\Delta\sigma_S$ is rather uniform throughout the area and mostly within 0.2. As shown in Figure S5, the non-uniform spatial distribution of $\Delta\sigma_S$ is preserved even when the 0–7 and 7–15 km depth intervals are considered.

A view of the seismic activity over the past 10 yr is provided by Figure 4e, which shows the spatial distribution of the cumulative of $\log(M_0)$ (hereinafter, all maps are computed considering the same grid and number of events per node used for $\Delta\sigma_S$). The most active segments turn out to be Marzano and the area beneath the Sele River Valley (located between Marzano and Cervialto faults), which acted as a barrier during the 1980 Irpinia earthquake (Cocco and Pacor, 1993). Again, the relative errors on the cumulative

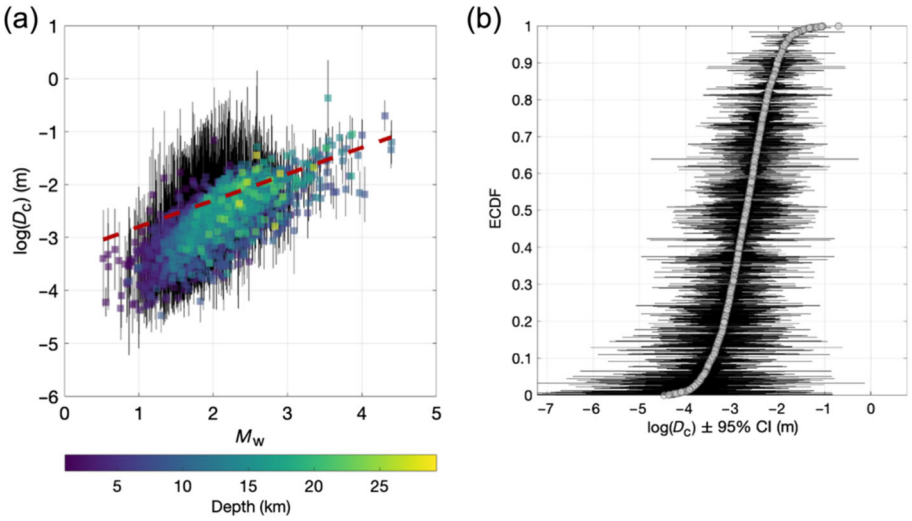

Figure 6. (a) Slip-weakening distance (D_c) versus M_w colored per depth and with the 95% probability CI. D_c versus M_0 scaling relation proposed by Ohnaka (2000) (the dashed red line). (b) ECDF for D_c with the 95% probability CI. The color version of this figure is available only in the electronic edition.

of M_0 are small and slightly larger in the southern part of the area (Fig. 4f).

Level II. Fracture energy (EG) and critical slip-weakening distance (DC)

Following the energy balance of the earthquake process and the simple scheme of the stress evolution with slip (Fig. 2a) proposed for small-magnitude earthquakes by Kanamori and Heaton (2000), we derive estimates of the fracture energy (E_G) and of the critical slip-weakening distance (D_c). The importance of these parameters for studying the dynamic of the rupture process through frictional sliding models is well known (e.g., Kanamori and Brodsky, 2004).

As with $\Delta\sigma_S$, for E_R, E_G, and D_c, we estimate the uncertainty (Fig. 5a,b) by propagating the errors affecting v and f_c (see Appendix). The spatial distribution of E and its uncertainty is shown in Figure 5c,d, respectively. Because E_G scales with M_0, to represent its spatial distribution, we remove such dependence as follows: (1) we divide the M_0 range into 10 bins, (2) for each bin, we compute the average of $\log(E_G)$, $\langle\log(E_G)\rangle$, (3) we compute the residuals between $\log(E_G)$ and the $\langle\log(E_G)\rangle$ relative to the M_0 bin to which the events belong. In this way, Figure 5c shows the spatial distribution of the excess or deficiency of the normalized E with respect to the mean of its ECDF (hereinafter, $\log(Z)$). This result suggests to us that the energy dissipation in the northern and southern Irpinia sectors is larger than in the central one.

The estimates of D_c are shown in Figure 6a. Our estimates range from a fraction of a millimeter to a few decimeters for the largest earthquakes at hand in our data set; these values are compatible with the ranges reported for earthquakes worldwide (e.g., see the review in Ohnaka, 2000, and references therein). In particular, for events with magnitude larger than about M_w 2.5, D_c values show a trend compatible with the scaling derived by Ohnaka (2000), which considered events with magnitude between $M_w \sim 2.5$ and $M_w \sim 8$. On the other hand, one has to consider that the uncertainty on D_c is very large (Fig. 6b). Therefore, for this parameter, we do not proceed further by analyzing its spatial distribution.

Level III. Seismological and geodetic measures

D'Agostino et al. (2018) studied geodetic displacement in the Irpinia area and showed that recharge of karst aquifers (0–3.5 km of depth) can produce poroelastic strain perturbations able to modulate the microseismicity occurrence rate. This type of connection reflects a high level of coupling of the Irpinia fault system, which D'Agostino (2014) found to be a general feature of the central and southern Apennines. Here, we consider the same Global Navigation Satellite Systems station (MRCV) used by D'Agostino et al. (2018) and compare its time series with time series of seismological parameters.

We start by performing a correlation analysis between the MRCV displacement, considering the composition of linearly detrended horizontal Global Positioning System time series in the anti-Apennine direction (i.e., N40°E), and the 90-day sliding average of the source dimension R (equation 5). For this first test, we limited the time period to the years 2008–2013, which both in terms of parameters and period shows a high level of similarity between seismological and geodetic time series. Our goal is, indeed, to understand how far in space we can extend the geodetic displacement estimates. Therefore, we consider events within a given hypocentral distance from MRCV (i.e., we explore the range of distances from 10 to 100 km, in 5 km steps), and for each of them we measure the Spearman's correlation between normalized geodetic displacement and R (Fig. S6). Our analysis suggests that for a wide range of distances (i.e., from 30 to 100 km) the level of correlation between the two observables is high. Therefore, in the following, we compare with geodetic displacement the seismological time series obtained considering events up to 100 km from MRCV, which in practice correspond to all of them.

Figure 7 shows the comparison of MRCV displacement (GeoDis) with the 90-day sliding average of (1) number of event (as in D'Agostino et al., 2018), (2) logarithm of M_0, (3) logarithm of S, (4) the source dimension, and (5) the logarithm of E. A similar plot for hypocentral depth is available in Figure S7, in which we show that the average depth of the events is relatively constant.

As previously observed (D'Agostino et al., 2018), there is a good correlation between the number of earthquakes, N, and the geodetic displacement (Fig. 7a). Regarding R and $\Delta\sigma_S$, they show a negative correlation with GeoDis in the period 2008–2013; after 2013, the correlation between parameters becomes less clear. In our view, remarkable is the correlation between GeoDis and the source dimension, which seems to hold from 2008 to 2016. Finally,

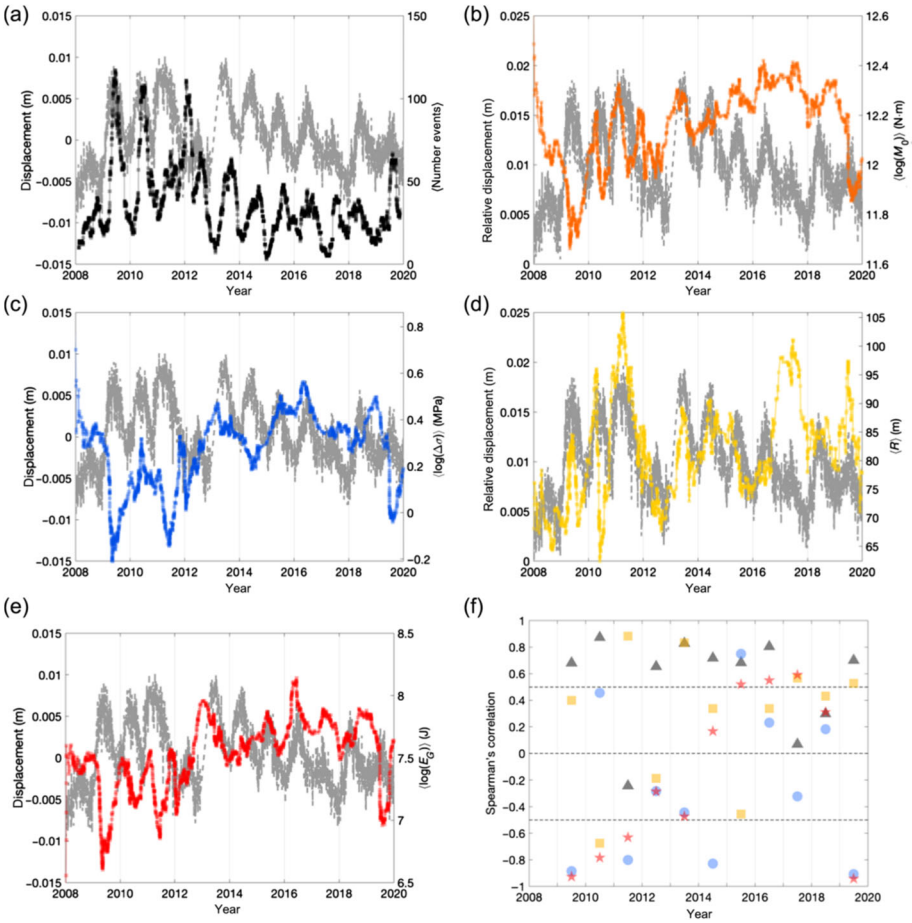

Figure 7. *Temporal evolution of geodetic displacement for the MRCV station (gray) versus different source parameters. (a) Number of events, (b) M_0, (c) $\Delta\sigma_S$, (d) source dimension R, and (e) E_G. (f) Temporal evolution of the Spearman's correlation coefficient for number of events (black), $\Delta\sigma_S$ (blue), E_G (red), and R (yellow) computed with respect to the geodetic displacement of the MRCV station. The color version of this figure is available only in the electronic edition.*

we observe that E shows a similar temporal trend to $\Delta\sigma_S$. We quantified the correlation of N, R, $\Delta\sigma_S$, and E with GeoDis through the Spearman's correlation by splitting the data for different years (Fig. 7f). The correlation between N, R, and GeoDis is generally positive, but time dependent. In contrast, $\Delta\sigma_S$ and E_G turn out to be anticorrelated to the geodetic displacement until 2013, but then they progressively correlate positively with it.

Our results indicate that the poroelastic strain perturbation generated by the karst aquifer recharge is not only able to modulate the microseismicity occurrence rate as proposed by D'Agostino et al. (2018) but can also lead to rupture asperities with different size and stress characteristics. Further studies will therefore be devoted to investigate and to model the connection between karst aquifer dynamics and microseismicity characteristics, as well as to define under which conditions a large earthquake could be generated.

DISCUSSION

Studying the source properties of microseismicity and their spatiotemporal evolution can allow the establishment of benchmarks for the background fault activity, seismicity pattern, seismic friction properties, and coupling. Microseismicity can thus allow intercepting preparation processes of large earthquakes, in which a stable and slow rupture growth develops into an unstable rupture within a confined zone around the future hypocenter (e.g., Bouchon et al., 2011; Schurr et al., 2014; Socquet et al., 2017; Tape et al., 2018).

Here, 10 yr long background seismicity recorded along the Irpinia fault system has been explored. We have focused on macroscopic source properties (i.e., M_0, f_c, and $\Delta\sigma_S$) estimated from the inversion of source spectra, and on parameters derived by the adoption of a simple frictional sliding model (i.e., E_G and D_c), which allows us to obtain indications about the local state of stress of faults. Our results, despite being related to the assumptions of the adopted models, describe a picture of the Irpinia area characterized by spatial and temporal variations of source parameters.

When we consider depths between 7 and 15 km (i.e., a depth range that includes the 1980 M_S 6.9 Irpinia earthquake), $\Delta\sigma_S$ varies between 1 and 10 MPa. These $\Delta\sigma_S$ values are therefore consistent with the 3.5 MPa value estimated for the M_S 6.9 Irpinia earthquake (Deschamps and King, 1983; Bernard and Zollo, 1989).

The spatial distribution of source parameters suggests a separation of the Irpinia fault system into three main sectors, related to the three main segments that were activated during the first two rupture episodes of the 1980 earthquake. The central sector is characterized by lower stress drop; the northern sector shows intermediate stress-drop values, whereas the largest values are observed in the southern sector (Fig. 5a). The spatial distribution of stress drop is not driven by the cumulative seismic moment on the fault structures. In fact, although the largest stress-drop values are observed in a region of lowest cumulated moment (southern sector), the variation in the stress drop is not mapped by changes in the cumulative moment. The largest moment release occurred at the boundaries of the lowest stress-drop area.

The tectonic complexity of the Irpinia region is well known (e.g., Bernard and Zollo, 1989; Ascione et al., 2013; Adinolfi et al., 2019). This region shows active, extensional faults arranged in subparallel structures, mainly disseminated over the Apennines axial sector, with trends ranging principally from west-northwest—east-southeast to northwest–southeast. The seismic active rock volume consists of the Apulian platform carbonates and its basement. The background microseismicity seems partly controlled by fluids of different origin (e.g., Chiodini et al., 2004;

Amoroso et al., 2014; Improta et al., 2014; D'Agostino et al., 2018).

The 3D velocity images and rock physical modeling of the Irpinia faults system (Amoroso et al., 2014; Improta et al., 2014; Vassallo et al., 2016; Amoroso et al., 2017) indicate that its central portion (i.e., roughly corresponding to the Marzano segment in which the 1980 Irpinia earthquake enucleated and the S. Gregorio immediately south of Marzano) has a porosity in carbonates around 4%–5% and a fluid composition consisting of brine–CO_2 and/or CH_4–CO_2. The northern sector (i.e., Cervialto fault, Fig. 1a), on the other hand, shows an approximately 20-km-long and 15-km-wide low-V_P/V_S anomaly between 6 and 10 km that is interpreted as a pressurized CO_2-rich rock volume within the Apulian platform carbonates (Improta et al., 2014). This velocity anomaly is also well correlated with high heat flow (100–215 mWm^{-2}) observed along the Mount Forcuso antiform and by a large natural emission of low-temperature CO_2-rich gases from nonvolcanic environment known as "Mefite d'Ansanto" (Chiodini et al., 2010).

The strong relationship between seismicity and high-pressure-deep CO_2-dominated fluids along the central and southern Apennines has been documented by several authors (Ghisetti and Vezzani, 2002; Chiodini et al., 2004; Chiarabba and Chiodini, 2013) and is believed to be responsible for the nucleation of large earthquakes (e.g., the 1997 Colfiorito and the 2009 L'Aquila seismic sequences, see Miller et al., 2004; Lucente et al., 2010). As pointed out by D'Agostino et al. (2018), however, fluids in karst aquifers following high multiannual recharge and intense seasonal rainfall can also lead to shallow poroelastic strain that can modulate deeper microseismicity and potentially induce large earthquakes.

The imprints of the spatial variability of $\Delta\sigma_S$ and of the cumulative M_0 lead E_G to show clear spatial patterns (Fig. 5), which could be related to the absence or presence of fluids, including those of different origin and composition, that plays a crucial role in the rupture dynamics by influencing the frictional properties of microruptures.

For magnitudes larger than M_w 2.5, D_c shows a trend compatible with the D_c versus M_0 scaling derived by Ohnaka (2000). This result suggests the suitability of the Ohnaka (2000) model for the Irpinia region and supports its use for realizing seismic hazard scenario studies. In contrast, smaller-magnitude events (i.e., M_w 2.5) show a D_c-over-M_0 trend deviating from Ohnaka's model. The reason for this trend is unclear. On one hand, the decrease in D_c could be due to the limited bandwidth affecting the estimation of radiated energy in the spectral domain (Ide and Beroza, 2001). As discussed by Bindi et al. (2020), several aspects play a role in determining the upper limit of the f_c estimate (e.g., near-surface attenuation and high variable $\Delta\sigma$). Therefore, although the explanatory power of the source model of Brune (1970) may support the estimation of f c near the limit of the analyzed bandwidth, we cannot exclude that our source parameter estimates may be progressively biased by attenuation effects for events with M_w < 2.

Our results are related to the use of simple source (e.g., Brune, 1970) and frictional (e.g., Kanamori and Heaton, 2000) models but, similarly to other studies carried out referring to such models (e.g., Abercrombie and Rice, 2005), our aim is to capture large-scale, collective behavior of micro and small seismicity that can provide information regarding the potential nucleation area of the next large earthquake.

Regarding the temporal evolution of microseismicity characteristics, we have observed a positive correlation between seismic source size and geodetic displacement in the period 2008–2016. Interestingly, both $\Delta\sigma_S$ and E_G are anticorrelated with the geodetic displacement in the period 2008–2014 but tend to progressively become positively correlated from 2017 to 2020. This result suggests that the energy required for the rupture process (EG) has changed over time, possibly due to a change in coupling. The observed temporal changes in geodetic displacement with respect to source parameters describing different aspects of rupture characteristics could indeed be related to changes in the seismic coupling of the Irpinia region.

Decoupling processes have been observed and studied prior megathrust earthquakes in subduction zones (e.g., Marsan et al., 2017 and Piña-Valdés et al., 2018, in Japan; Schurr et al., 2014 and Socquet et al., 2017, for Chile). For the 2014 Chile megathrust, for example, Socquet et al. (2017) reported an eight-month preparatory phase in which reduced coupling was associated with fluid migration within the fault zone, with a progressive expansion of ruptures into conditionally stable areas (Lay et al., 2012) confined around the mainshock hypocenter. We are currently unable to provide coupling estimates for the Irpinia region. Future studies will therefore be directed toward implementing the procedure proposed by Dublanchet (2019), which allows seismic coupling to be obtained and monitored by comparing seismological and geodetic displacement measurements.

CONCLUSION

In this work, we showed that parameters describing different aspects of microearthquake seismic ruptures can be combined to characterize the heterogeneous behavior of the Irpinia faults system. Of course, as is always the case when dealing with the interpretation of source parameters, all results are related to the assumptions of the adopted models (i.e., source model of Brune, 1970 and stress-release model by Kanamori and Heaton, 2000). However, we think that the spatial and temporal variations of source parameters obtained in this work can be very useful for monitoring the stress conditions of the Irpinia fault and provide meaningful information for conducting hazard studies.

The results of our analyses can be summarized as follows:

Level I—f_c and M_0 estimates show depth dependency. Events at hypocentral depth less than 7 km are characterized by smaller $\Delta\sigma_S$ than those in the depth range of 7–15 km. The latter, which includes the hypocenter of the 1980 Irpinia earthquake, was the main focus of our study. Our results indicate that $\Delta\sigma_S$ for the deepest events varies

between 1 and 10 MPa. Interestingly, the variability of $\Delta\sigma_S$ outlines clear spatial patterns of fault mechanical properties, suggesting that the Irpinia fault system can be divided into three main sectors and that those to the north (Cervialto) and south (Melandro–Pergola) show higher stress values than the central one (Marsano).

Level II—Estimates of fracture energy, E_G, and slip-weakening distance, D_c, derived by applying the Kanamori and Heaton (2000) slip model show that the three sectors present distinct dynamic characteristics. These results are likely due to the presence of fluids with different composition in the volume of the Cervialto (CO_2 dominated) and Marzano (brine–CO_2 and/or CH_4–CO_2) faults. D_c estimates for larger magnitude events (M_w > 2:5) present a trend with M_0 compatible with that derived by Ohnaka (2000) for large earthquakes. Of course, this may be an important constraint for the realization of scenario studies of large earthquakes in the Irpinia region.

Level III—The microseismicity in Irpinia shows a high level of correlation with geodetic displacement measurements (either positive or negative correlation depending on the source parameter considered) for the period 2008–2013. D'Agostino et al. (2018) demonstrated that recharge of karst aquifers can modulate the occurrence rate of microseismicity. In this study, we showed that this phenomenon is also able to influence the dynamic characteristics of microseismicity. In addition, we observed that a temporal change in the relationship between the geodetic displacement and seismic source parameters occurred after 2014. Further analyses are needed to understand the origin of the observed changes in the dynamic characteristics of the microseismicity. Indeed, we think that 4D velocity and attenuation tomography could provide insight into whether the observed changes are related to fluid inclusion and migration in this area. Additional areas for further investigation include the impact of the seismic attenuation on the depth dependence of stress drop, an issue on which recent studies have provided contrasting results (e.g., Abercrombie et al., 2021; Bindi et al., 2021).

Several recent studies (Schurr et al., 2014; Socquet et al., 2017; Tape et al., 2018; Dresen et al., 2020; Kato and Ben-Zion, 2020; Picozzi and Iaccarino, 2021) have shown that large earthquakes can be preceded by a preparatory phase in which a stable and slow rupture growth develops into unstable rupture within a confined zone around the future hypocenter. With respect to this scientific challenge, we believe that near-fault observatories and analyses such as those presented in this work, in which we characterized microseismicity in terms of different parameters and we compared them with geodetic displacement, can be a powerful means for unveiling the preparatory processes of large earthquakes.

DATA AND RESOURCES

Publicly available data sets were analyzed in this study, available at http://isnet-bulletin.fisica.unina.it/cgi-bin/isnet-events/isnet.cgi. The analysis has been performed using MATLAB software (R2019b, https://it.mathworks.com/). Data about Irpinia Near-Fault Observatory (INFO) are available at https://www.epos-eu.org/. Information about Irpinia Seismic Network (ISNet) is available at http://isnet.unina.it. All websites were last accessed in July 2021. The supplemental material includes 37 figures that provide additional information regarding the empirical attenuation functions and site responses from generalized inversion technique (GIT) inversion, corner frequency scaling with seismic moment for two depth ranges, and stress-drop distribution with moment magnitude and its uncertainties.

DECLARATION OF COMPETING INTERESTS

The authors acknowledge that there are no conflicts of interest recorded.

ACKNOWLEDGMENTS

The data products and the provision of services in this research are funded by Ministero Università e Ricerca (MIUR), through the project European Plate Observing System (EPOS)-Italia, and by Dipartimento di Protezione Civile (DPC), through a collaboration agreement with the University of Naples Federico II. Part of the research was funded by the national project Progetti di Rilevante Interesse Nazionale (PRIN) Detection and tracking of crustal fluid by multi-parametric methodologies and technologies (FLUIDS) (Grant Number 20174 × 3P29). The authors thank the RISSCLab team for the earthquakes data set preparation and G. De Landro for the vertical and horizontal location error estimates.

REFERENCES

Abercrombie, R. E., and J. R. Rice (2005). Can observations of earthquake scaling constrain slip weakening? Geophys. J. Int. 2005, no. 162, 406–424, doi: 10.1111/j.1365-246x.2005.02579.x

Abercrombie, R. E., D. T. Trugman, P. M. Shearer, X. Chen, J. Zhang, C. N. Pennington, J. L. Hardebeck, T. H. W. Goebel, and C. J. Ruhl (2021). Does earthquake stress drop increase with depth in the crust? J. Geophys. Res. doi: 10.1002/essoar.10506989.1.

Adinolfi, G. M., S. Cesca, M. Picozzi, S. Heimann, and A. Zollo (2019). Detection of weak seismic sequences based on arrival time coherence and empiric network detectability: An application at a near fault observatory, Geophys. J. Int. 218, no. 3, 2054–2065.

Amoroso, O., A. Ascione, S. Mazzoli, J. Virieux, and A. Zollo (2014). Seismic imaging of a fluid storage in the actively extending Apennine mountain belt, southern Italy, Geophys. Res. Lett. 41, 3802–3809, doi: 10.1002/2014GL060070.

Amoroso,O., G. Russo, G. De Landro, A. Zollo, S. Garambois, S. Mazzoli, M. Parente, and J. Virieux (2017). From velocity and attenuation tomography to rock physical modeling: Inferences on fluid-driven earthquake processes at the Irpinia fault system in southern Italy, Geophys. Res. Lett. 44, 6752–6760, doi: 10.1002/2016GL072346.

Anderson, J. G., and S. Hough (1984). A model for the shape of the Fourier amplitude spectrum of acceleration at high frequencies, Bull. Seismol. Soc. Am. 74, no. 5, 1969–1993.

Ascione, A., S. Mazzoli, P. Petrosino, and E. Valente (2013). A decoupled kinematic model for active normal faults: Insights from the 1980, MS _ 6:9 Irpinia earthquake, southern Italy. Geol. Soc. Am. Bull. 125, 1239–1259, doi: 10.1130/B30814.1.

Baltay, A. S., T. C. Hanks, and G. C. Beroza (2013). Stable stress-drop measurements and their variability: Implications for ground-motion prediction, Bull. Seismol. Soc. Am. 103, no. 1, 211–222, doi: 10.1785/0120120161.

Bello, S., R. deNardis, R. Scarpa, F. Brozzetti,D. Cirillo, F. Ferrarini, B. di Lieto, R. J. Arrowsmith, and G. Lavecchia (2021). Fault pattern and seismotectonic style of the Campania–Lucania 1980 earthquake (M_w 6.9, southern Italy): New multidisciplinary constraints, Front. Earth Sci. 8, 608,063, doi: 10.3389/feart.2020.608063.

Bentz, S., G. Kwiatek, P. Martínez-Garzón, M. Bohnhoff, and G. Dresen (2020). Seismic moment evolution during hydraulic stimulations, Geophys. Res. Lett. 47, e2019GL086185, doi: 10.1029/2019GL086185.

Bernard, P., and A. Zollo (1989). The Irpinia (Italy) 1980 earthquake: Detailed analysis of a complex normal fault, J. Geophys. Res. 94, 1631–1648.

Bindi, D., F. Cotton, D. Spallarossa, M. Picozzi, and E. Rivalta (2018). Temporal variability of ground shaking and stress drop in central Italy: A hint for fault healing? Bull. Seismol. Soc. Am. 108, no. 4, 1853–1863, doi: 10.1785/0120180078.

Bindi, D., H. N. T. Razafindrakoto, M. Picozzi, and A. Oth (2021). Stress drop derived from spectral analysis considering the hypocentral depth in the attenuation model: Application to the Ridgecrest region, California, Bull. Seismol. Soc. Am. doi: 10.1785/0120210039.

Bindi, D., D. Spallarossa, M. Picozzi, and P. Morasca (2020). Reliability of source parameters for small events in central Italy: Insights from spectral decomposition analysis applied to both synthetic and real data, Bull. Seismol. Soc. Am. 110, 3139–3157, doi: 10.1785/0120200126.

Boore, D. M. (1983). Stochastic simulation of high-frequency ground motions based on seismological models of the radiated spectra, Bull. Seism. Soc. Am. 73, 1865–1894.

Boore, D. M. (2003). Some notes on phase derivatives and simulating strong ground motions, Bull. Seismol. Soc. Am. 93, 1132–1143.

Boore, D. M., and J. Boatwright (1984). Average body-wave radiation coefficients, Bull. Seismol. Soc. Am. 74, 1615–1621.

Bouchon, M., H. Karabulut, M. Aktar, S. Özalaybey, J. Schmittbuhl, and M.-P. Bouin (2011). Extended nucleation of the 1999 M_w 7.6 Izmit earthquake, Science 331, no. 6019, 877–880, doi: 10.1126/science.1197341.

Brune, J. N. (1970). Tectonic stress and the spectra of seismic shear waves from earthquakes, J. Geophys. Res. 75, 4997–5009, doi: 10.1029/jb075i026p04997.

Burrato, P., and G. Valensise (2008). Rise and fall of a hypothesized seismic gap: Source complexity in the Mw 7.0 16 December 1857 southern Italy earthquake, Bull. Seismol. Soc. Am. 98, no. 1, 139–148, doi: 10.1785/0120070094.

Cantore, L., A. Oth, S. Parolai, and D. Bindi (2011). Attenuation, source parameters and site effects in the Irpinia–Basilicata region (southern Apennines, Italy), J. Seismol. 15, 375–389, doi: 10.1007/s10950-011-9230-2.

Castro, R. R., J. G. Anderson, and S. K. Singh (1990). Site response, attenuation and source spectra of S waves along the Guerrero, Mexico, subduction zone, Bull. Seismol. Soc. Am. 80, no. 6, 1481–1503.

Causse, M., and S. G. Song (2015). Are stress drop and rupture velocity of earthquakes independent? Insight from observed ground motion variability, Geophys. Res. Lett. 42, 7383–7389, doi: 10.1002/2015GL064793.

Chen, X., and R. E. Abercrombie (2020). Improved approach for stress drop estimation and its application to an induced earthquake sequence in Oklahoma, Geophys. J. Int. 223, no. 1, 233–253, doi: 10.1093/gji/ggaa316.

Chiarabba, C., and G. Chiodini (2013). Continental delamination and mantle dynamics drive topography, extension and fluid discharge in the Apennines, Geology 41, 715–718, doi: 10.1130/g33992.1.

Chiarabba, C., P. De Gori, M. Segou, and M. Cattaneo (2020). Seismic velocity precursors to the 2016 Mw 6.5 Norcia (Italy) earthquake, Geology 48, doi: 10.1130/G47048.1.

Chiarabba, C., L. Jovane, and R. Distefano (2005). A new view of Italian seismicity using 20 years of instrumental recordings, Tectonophysics 395, 251–268, doi: 10.1016/j.tecto.2004.09.013.

Chiodini, G., C. Cardellini, A. Amato, E. Boschi, S. Caliro, F. Frondini, and G. Ventura (2004). Carbon dioxide Earth degassing and seismogenesis in central and southern Italy, Geophys. Res. Lett. 31, L07615, doi: 10.1029/2004GL019480.

Chiodini, G., D. Granieri, R. Avino, S. Caliro, A. Costa, C. Minopoli, and G. Vilardo (2010). Non-volcanic CO2 Earth degassing: Case of Mefite d'Ansanto (southern Apennines), Italy, Geophys. Res. Lett. 37, L11303, doi: 10.1029/2010GL042858.

Cocco, M., and F. Pacor (1993). The rupture process of the 1980 Irpinia, Italy, earthquake from the inversion of strong motion waveforms, Tectonophysics 218, 157–177.

Cotton, F., R. Archuleta, and M. Causse (2013). What is the sigma of stress drop?, Seismol. Res. Lett. 84, 42–48, doi: 10.1785/0220120087.

D'Agostino, N. (2014). Complete seismic release of tectonic strain and earthquake recurrence in the Apennines (Italy), Geophys. Res. Lett. 41, 1155–1162, doi: 10.1002/2014GL059230.

D'Agostino, N., F. Silverii, O. Amoroso, V. Convertito, F. Fiorillo, G. Ventafridda, and A. Zollo (2018). Crustal deformation and seismicity modulated by groundwater recharge of karst aquifers, Geophys. Res. Lett. 45, 12,253–12,262, doi: 10.1029/2018GL079794.

De Landro, G., O. Amoroso, T. A. Stabile, E. Matrullo, A. Lomax, and A. Zollo (2015). High-precision differential earthquake location in 3-D models: Evidence for a rheological barrier controlling the microseismicity at the Irpinia fault zone in southern Apennines, Geophys. J. Int. 203, 1821–1831.

Denolle, M. A., and P. M. Shearer (2016). New perspectives on self-similarity for shallow thrust earthquakes, J. Geophys. Res. 121, no. 9, 6533–6565, doi: 10.1002/2016JB013105.

Deschamps, A., and G. C. P. King (1983). The Campania–Lucania (southern Italy) earthquake of 23 November 1980, Earth Planet. Sci. Lett. 62, 296–304.

Dresen, G., G. Kwiatek, T. Goebel, and Y. Ben-Zion (2020). Seismic and aseismic preparatory processes before large stick–slip failure, Pure Appl. Geophys. 177, 5741–5760.

Dublanchet, P. (2019). Inferring fault slip rates from cumulative seismic moment in a multiple asperity context, Geophys. J. Int. 216, no. 1, 395–413, doi: 10.1093/gji/ggy431.

Durand, V., S. Bentz, G. Kwiatek, G. Dresen, C. Wollin, O. Heidbach, P. Martínez-Garzòn, F. Cotton, M. Nurlu, and M. Bohnhoff (2020). A two-scale preparation phase preceded an M_w 5.8 earthquake in the Sea of Marmara offshore Istanbul, Turkey, Seismol. Res. Lett. 91, no. 6, 3139–3147, doi: 10.1785/0220200110.

Efron, B. (1979). Bootstrap methods: another look at the jackknife, Ann. Stat. 7, no. 1, 1–26.

Eshelby, J. D. (1957). The determination of the elastic field of an ellipsoidal inclusion, and related problems, Proc. Math. Phys. Sci. 241, 376–396.

Festa, G., G. M. Adinolfi, A. Caruso, S. Colombelli, G. De Landro, L. Elia, A. Emolo, M. Picozzi, A. Scala, F. Carotenuto, et al. (2021). Insights into mechanical properties of the 1980 Irpinia fault system from the analysis of a seismic sequence. Geosciences 11, 28, doi: 10.3390/geosciences11010028.

Ghisetti, F., and L. Vezzani (2002). Normal faulting, transcrustal permeability and seismogenesis in the Apennines (Italy), Tectonophysics 348, 155–168.

Goertz-Allmann, B. P., A. Goertz, and S. Wiemer (2011). Stress drop variations of induced earthquakes at the Basel geothermal site, Geophys. Res. Lett. 38, L09308, doi: 10.1029/2011GL047498.

Hanks, T. C., and W. Thatcher (1972). A graphical representation of seismic source parameters, J. Geophys. Res. 77, no. 23, 4393–4405, doi: 10.1029/JB077i023p04393.

Hartzell, S., P. Liu, and C. Mendoza (1996). The 1994 Northridge, California, earthquake: Investigation of rupture velocity, risetime, and high-frequency radiation, J. Geophys. Res. 101, 20,091–20,108.

Iannaccone, G., A. Zollo, L. Elia, V. Convertito, C. Satriano, C. Martino, G. Festa, M. Lancieri, A. Bobbio, T. A. Stabile, et al. (2010). A prototype system for earthquake early-warning and alert man-agement in southern Italy, Bull. Earth Eng. 8, 1105–1129, doi: 10.1007/s10518-009-9131-8.

Ide, S., and G. C. Beroza (2001). Does apparent stress vary with earthquake size?, Geophys. Res. Lett. 28, 3349–3352, doi: 10.1002/2013JB010890.

Improta, L., P. De Gori, and C. Chiarabba (2014). New insights into crustal structure, Cenozoic magmatism, CO2 degassing, and seismogenesis in the southern Apennines and Irpinia region from local earthquake tomography, J. Geophys. Res. 119, 8283–8311, doi: 10.1002/2013JB010890.

Izutani, Y., and H. Kanamori (2001). Scale-dependence of seismic energy-to-moment ratio for strike-slip earthuakes in Japan, Geophys. Res. Lett. 28, 4007–4010, doi: 10.1029/2001GL013402.

Kanamori, H., and E. E. Brodsky (2004). The physics of earthquakes, Rep. Progr. Phys. 67, 1429–1496, doi: 10.1088/0034-4885/67/8/R03.

Kanamori, H., and T. H. Heaton (2000). Microscopic and macroscopic physics of earthquakes, in Geocomplexity and the Physics of Earthquakes, J. B. Rundle, D. L. Turcotte, and W. Klein (Editors), doi: 10.1029/GM120p0147.

Kanamori, H., and L. Rivera (2004). Static and dynamic scaling relations for earthquakes and their implications for rupture speed and stress drop, Bull. Seismol. Soc. Am. 94, 314–319.

Kato, A., and Y. Ben-Zion (2020). The generation of large earthquakes, Nat. Rev. Earth Environ. 2, 26–39, doi: 10.1038/s43017-020-00108-w.

Kawase, H. (2006). Site effects derived from spectral inversion method for K-NET, KiK-net, and JMA strong-motion network with special reference to soil nonlinearity in high PGA records, Bull. Earthq. Res. Inst. 81, 309–315.

Kwiatek, G., and Y. Ben-Zion (2016). Theoretical limits on detection and analysis of small earthquakes, J. Geophys. Res. 121, 5898–5916, doi: 10.1002/2016JB012908.

Kwiatek, G., F. Bulut, M. Bohnhoff, and G. Dresen (2014). Highresolution analysis of seismicity induced at Berlín geothermal field, El Salvador, Geothermics 52, 98–111, doi: 10.1016/j.geothermics.2013.09.008.

Kwiatek, G., K. Plenkers, and G. Dresen (2011). Source parameters of picoseismicity recorded at Mponeng deep gold mine, South Africa: Implications for scaling relations, Bull. Seismol. Soc. Am. 101, no. 6, 2592–2608, doi: 10.1785/0120110094.

Lay, T., H. Kanamori, C. J. Ammon, K. D. Koper, A. R. Hutko, L. Ye, H. Yue, and T. M. Rushing (2012). Depth-varying rupture properties of subduction zone megathrust faults, J. Geophys. Res. 117, no. B04311, doi: 10.1029/2011JB009133.

Lucente, F. P., P. De Gori, D. Piccini, M. Di Bona, C. Chiarabba, and N. Piana Agostinetti (2010). Temporal variation of seismic velocity and anisotropy before the 2009 Mw 6.3 L'Aquila earthquake, Italy, Geology 38, no. 11, 1015–1018, doi: 10.1130/G31463.1.

Marsan, D., M. Bouchon, B. Gardonio, H. Perfettini, A. Socquet, and B. Enescu (2017). Change in seismicity along the Japan trench, 1990–2011, and its relationship with seismic coupling, J. Geophys. Res. 122, 4645–4659, doi: 10.1002/2016JB013715.

Matrullo, E., R. De Matteis, C. Satriano, O. Amoroso, and A. Zollo (2013). An improved 1-D seismic velocity model for seismological studies in Campania–Lucania region (southern Italy), Geophys. J. Int. 195, 460–473.

Miller, S. A., C. Collettini, L. Chiaraluce, M. Cocco, M. Barchi, and B. J. Kaus (2004). Aftershocks driven by high-pressure CO2 source at depth, Nature 427, no. 6976, 724–727, doi: 10.1038/nature02251.

Orowan, E. (1960). Mechanism of seismic faulting, Geol. Soc. Am. Memoir 79, 323–345.

Ohnaka, M. (2000). A physical scaling relation between the size of an earthquake and its nucleation zone size, Pure Appl. Geophys. 157, 2259–2282.

Oth, A. (2013). On the characteristics of earthquake stress release variations in Japan, Earth Planet. Sci. Lett. 377/378, 132–141, doi: 10.1016/j.epsl.2013.06.037.

Oth, A., D. Bindi, S. Parolai, and D. D. Giacomo (2011). Spectral analysis of K-NET and KIK-net data in Japan. Part II: On attenuation characteristics, source spectra, and site response of borehole and surface stations, Bull. Seismol. Soc. Am. 101, no. 2, 667–687.

Oth, A., H. Miyake, and D. Bindi (2017). On the relation of earthquake stress drop and ground motion variability, J. Geophys. Res. 122, 5474–5492, doi: 10.1002/2017JB014026.

Pacor, F., D. Spallarossa, A. Oth, L. Luzi, R. Puglia, L. Cantore, A. Mercuri, M. D'Amico, and D. Bindi (2016). Spectral models for ground motion prediction in the L'Aquila region (central Italy): Evidence for stress-drop dependence on magnitude and depth, Geophys. J. Int. 204, no. 2, 697–718, doi: 10.1093/gji/ggv448.

Paige, C. C., and M. A. Saunders (1982). LSQR: An algorithm for sparse linear equations and sparse least squares, ACM Trans. Math Software 8, no. 1, 43–71.

Picozzi, M., and A. G. Iaccarino (2021). Forecasting the preparatory phase of induced earthquakes by recurrent neural network, Forecasting 3, 17–36, doi: 10.3390/forecast3010002.

Picozzi, M., D. Bindi, A. Zollo, G. Festo, and D. Spallarossa (2019). Detecting long-lasting transients of earthquake activity on a fault system by monitoring apparent stress, ground motion and clustering, Sci. Rep. 9, 16,268, doi: 10.1038/s41598-019-52756-8.

Picozzi, M., A. Oth, S. Parolai, D. Bindi, G. De Landro, and O. Amoroso (2017). Accurate estimation of seismic source parameters of induced seismicity by a combined approach of generalized inversion and genetic algorithm: Application to the Geysers geothermal area, California, J. Geophys. Res. 122, doi: 10.1002/2016JB013690.

Piña-Valdés, J., A. Socquet, and F. Cotton (2018). Insights on the Japanese subduction megathrust properties from depth and lateral variability of observed ground motions, J. Geophys. Res. 123, no. 10, 8937–8956, doi: 10.1029/2018JB015743.

Ross, Z. E., and Y. Ben-Zion (2016). Towards reliable automated estimates of earthquake source properties from body wave spectra, J. Geophys. Res. 121, 4390–4407, doi: 10.1002/2016JB013003.

Savage, J. C., and M. D. Wood (1971). The relation between apparent stress and stress drop, Bull. Seismol. Soc. Am. 61, 1381–1388.

Schurr, B., G. Asch, S. Hainzl, J. Bedford, A. Hoechner, M. Palo, R. Wang, M. Moreno, M. Bartsch, Y. Zhang, et al. (2014). Gradual unlocking of plate boundary controlled initiation of the 2014 Iquique earthquake, Nature 512, 299–302, doi: 10.1038/nature13681.

Shearer, P. M., G. A. Prieto, and E. Hauksson (2006). Comprehensive analysis of earthquake source spectra in southern California, J. Geophys. Res. 111, no. B06303, doi: 10.1029/2005JB003979.

Socquet, A., J. Piña-Valdes, J. Jara, F. Cotton, A. Walpersdorf, N. Cotte, S. Specht, F. Ortega-Culaciati, D. Carrizo, and E. Norabuena (2017). An 8 month slow slip event triggers progressive nucleation of the 2014 Chile megathrust, Geophys. Res. Lett. 44, no. 9, 4046–4053.

Stabile, T. A., C. Satriano, A. Orefice, G. Festa, and A. Zollo (2012). Anatomy of a microearthquake sequence on an active normal fault, Sci. Rep. 2, no. 410, 1–7, doi: 10.1038/srep00410.

Sugan, M., A. Kato, H. Miyake, S. Nakagawa, and A. Vuan (2014). The preparatory phase of the 2009 Mw 6.3 L'Aquila earthquake by improving the detection capability of low-magnitude foreshocks, Geophys. Res. Lett. 41, 6137–6144, doi: 10.1002/2014GL061199.

Tape, C., S. Holtkamp, V. Silwal, J. Hawthorne, Y. Kaneko, J. P. Ampuero, C. Ji, N. Ruppert, K. Smith, and M. E. West (2018). Earthquake nucleation and fault slip complexity in the lower crust of central Alaska, Nature Geosci. 11, 536–541, doi: 10.1038/s41561-018-0144-2.

Terakawa, T., A. Zoporowski, B. Galvan, and S. A. Miller (2010). High-pressure fluid at hypocentral depths in the L'Aquila region inferred from earthquake focal mechanisms, Geology 38, 995–998, doi: 10.1130/G31457.1.

Trugman, D. T. (2020). Stress-drop and source scaling of the 2019 ridgecrest, California, earthquake sequence, Bull. Seismol. Soc. Am. 110, 1859–1871, doi: 10.1785/0120200009.

Tsuda, K., K. Koketsu, Y. Hisada, and T. Hayakawa (2010). Inversion analysis of site responses in the Kanto basin using data from a dense strong motion seismograph array, Bull. Seismol. Soc. Am. 100, no. 3, 1276–1287, doi: 10.1785/0120090153.

Vassallo, M., G. Festa, and A. Bobbio (2012). Seismic ambient noise analysis in southern Italy, Bull. Seismol. Soc. Am. 102, no. 2, 574–586, doi: 10.1785/0120110018.

Vassallo, M., G. Festa, A. Bobbio, and M. Serra (2016). Low shear velocity in a normal fault system imaged by ambient noise cross correlation: The case of the Irpinia fault zone, southern Italy, J. Geophys. Res. 121, 4290–4305, doi: 10.1002/2015JB012410.

Udías, A. V., R. Madariaga, and E. Buforn (2014). Source Mechanisms of Earthquakes: Theory and Practice, Cambridge, Cambridge University Press, New York, New York.

Wang, H., Y. Ren, R. Wen, and P. Xu (2019). Breakdown of earthquake self-similar scaling and source rupture directivity in the 2016–2017 central Italy seismic sequence, J. Geophys. Res. 124, 3898–3917, doi: 10.1029/2018JB016543.

Wiemer, S. (2001). A software package to analyze seismicity: ZMAP, Seismol. Res. Lett. 72, 373–382.

Wiemer, S., and M. Wyss (2002). Mapping spatial variability of the frequency–magnitude distribution of earthquakes, Adv. Geophys. 45, 259–302, doi: 10.1016/S0065-2687(02)80007-3.

Wyss, M., and J. N. Brune (1968). Seismic moment, stress, and source dimensions for earthquakes in the California–Nevada region, J. Geophys. Res. 73, 4681–4694.

Yamanaka, H., and H. Ishida (1996). Application of GENERIC algorithms to an inversion of surface-wave dispersion data, Bull. Seismol. Soc. Am. 86, 436–444.

Zollo, A., A. Orefice, and V. Convertito (2014). Source parameter scaling and radiation efficiency of microearthquakes along the Irpinia fault zone in southern Apennines, Italy, J. Geophys. Res. 119, 3256–3275, doi: 10.1002/2013JB010116.

APPENDIX

Considering the standard deviation on f c and M0 (sf c and sM0), the error propagation on ΔσS is carried out similarly to Cotton et al. (2013) using the variance formula, truncated at the first order of the Taylor's expansion:

$$s\Delta\sigma_S = \left(\left(\frac{3\text{const} M_0 f_c^2}{V_S^3} \right)^2 sf_c^2 + \left(\frac{\text{const} f_c^3}{V_S^3} \right)^2 sM_0^2 \right)^{(1/2)} . \quad \text{(A1)}$$

With respect to Bindi et al. (2018), we neglected the cross term of the covariance matrix (as Cotton et al., 2013), which results in a conservative choice.

Following Udías et al. (2014), the radiated energy (equation 7) can be expressed as

$$E_S = \left(\frac{\langle R^c \rangle 2}{16\pi\rho c^5}\right) M_0^2 \omega_c^3. \quad \text{(A2)}$$

The standard deviation sE_S is thus computed as

$$sE_S = ((3\text{const}M_0^2\omega_c^2)^2 sf_c^2 + (2\text{const}M_0\omega_c^3)^2 sM_0^2)^{(1/2)}. \quad \text{(A3)}$$

Then, considering equation (9), we compute the standard deviation sE_G as

$$sE_S = \left(\left(\frac{\Delta\sigma_S}{2\mu}\right)^2 sM_0^2 + \left(\frac{M_0}{2\mu}\right)^2 s\Delta\sigma_S^2 + (1)^2 sE_S^2\right)^{\left(\frac{1}{2}\right)}. \quad \text{(A4)}$$

Finally, considering equation (10) and for all the earthquakes in a circular fault of areas (i.e., S _ πR2), we compute the standard deviations SDc as

$$sD_c = \left(\left(\frac{2}{\Delta\sigma_S S}\right)^2 sE_G^2 + \left(\frac{2E_G}{\Delta\sigma_S S^2}\right)^2 sS^2 + \left(\frac{2E_G}{\Delta\sigma_S^2 S}\right)^2 sE_G^2\right)^{\left(\frac{1}{2}\right)}. \quad \text{(A5)}$$